The Rad50 hook domain regulates DNA damage signaling and tumorigenesis

Ramon Roset,[1] Akiko Inagaki,[1] Marcel Hohl,[1] Fabienne Brenet,[2] Julien Lafrance-Vanasse,[3] Julian Lange,[1] Joseph M. Scandura,[2] John A. Tainer,[3] Scott Keeney,[1,4,5] and John H.J. Petrini[1,5,6]

[1]Molecular Biology Program, Memorial Sloan-Kettering Cancer Center, New York, New York 10021, USA; [2]Department of Medicine, Laboratory of Molecular Hematopoiesis, Weill-Cornell Medical College, New York, New York 10065, USA; [3]Life Sciences Division, Lawrence Berkeley National Laboratory, Berkeley, California 94720, USA; [4]Howard Hughes Medical Institute, Memorial Sloan-Kettering Cancer Center, New York, New York 10065, USA; [5]Weill Graduate School of Medical Sciences, Cornell University, New York, New York 10021, USA

The Mre11 complex (Mre11, Rad50, and Nbs1) is a central component of the DNA damage response (DDR), governing both double-strand break repair and DDR signaling. Rad50 contains a highly conserved Zn^{2+}-dependent homodimerization interface, the Rad50 hook domain. Mutations that inactivate the hook domain produce a null phenotype. In this study, we analyzed mutants with reduced hook domain function in an effort to stratify hook-dependent Mre11 complex functions. One of these alleles, $Rad50^{46}$, conferred reduced Zn^{2+} affinity and dimerization efficiency. Homozygous $Rad50^{46/46}$ mutations were lethal in mice. However, in the presence of wild-type $Rad50$, $Rad50^{46}$ exerted a dominant gain-of-function phenotype associated with chronic DDR signaling. At the organismal level, $Rad50^{+/46}$ exhibited hydrocephalus, liver tumorigenesis, and defects in primitive hematopoietic and gametogenic cells. These outcomes were dependent on ATM, as all phenotypes were mitigated in $Rad50^{+/46}$ $Atm^{+/-}$ mice. These data reveal that the murine Rad50 hook domain strongly influences Mre11 complex-dependent DDR signaling, tissue homeostasis, and tumorigenesis.

The Mre11 complex is a large multicomponent assembly that comprises two Mre11, two Rad50, and two Nbs1 (Xrs2 in *Saccharomyces cerevisiae*) molecules that plays a central role in the DNA damage response (DDR). The complex consists of a globular domain in which Mre11 and Nbs1 associate with the Walker A and B domains of Rad50 (Fig. 1A). A large coiled-coil domain of Rad50 extends out from the globular domain and folds back on itself in an anti-parallel manner, with the Rad50 hook domain at the apex. The hook domain is a highly conserved interface that mediates homotypic dimerization via the coordination of a Zn^{2+} atom by two invariant cysteines from each of two Rad50 protomers (Hopfner et al. 2002).

The Mre11 complex is a sensor of DNA double-strand breaks (DSBs) that is required for DDR signaling primarily via the kinase ATM (Stracker and Petrini 2011). Recent data suggest that the complex may also influence the activation of ATR, which is primarily activated in response to DNA replication stress (Stiff et al. 2005; Duursma et al. 2013; Shiotani et al. 2013). These observations underlie the view that the Mre11 complex plays an integral role in the regulation of signaling within the DDR network.

The Mre11 complex plays a key role in DSB repair, promoting both homology-directed DSB repair (HDR) and nonhomologous end-joining (NHEJ). With respect its role in HDR, genetic and physical evidence suggests that the primary function of the Mre11 complex is to promote HDR between sister chromatids via the hook and coiled-coil domains of Rad50 (Bressan et al. 1999; Hartsuiker et al. 2001; Gonzalez-Barrera et al. 2003; Wiltzius et al. 2005; Hohl et al. 2011). Mre11 complex-mediated NHEJ appears to be primarily dependent on DNA-binding sites in the globular domain (Williams et al. 2008, 2009), although we showed that the hook and coiled-coil domains also influence this process, presumably via long-range effects on the disposition of globular domain components (Hohl et al. 2011).

[6]Corresponding author
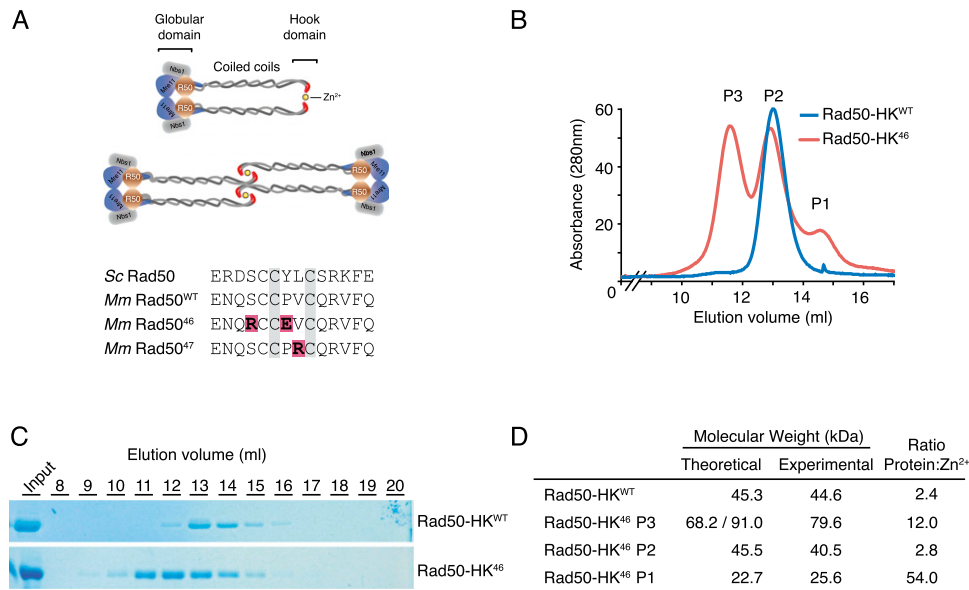E-mail petrinij@mskcc.org

Figure 1. Analysis of Rad50 hook dimerization. (*A*, *top* panel) Schematic representation of the Mre11 complex in two possible configurations. Rad50 globular domain shown in brown, Mre11 is in blue, and Nbs1 is in gray. (*Bottom* panel) Sequence of the hook domain from *S. cerevisiae*, *Mus musculus*, and the *Rad50^46* and *Rad50^47* mutants. (*B*) Gel filtration profile of Rad50-HK proteins. (*C*) Fractions from *B* were resolved on an acrylamide gel and stained with Coomassie. (*D*) Molecular weight and Zn^{2+} content of the indicated Rad50-HK proteins determined by SEC-MALS and ICP-MS, respectively. Theoretical molecular weight for a monomeric (P1), dimeric (P2 and Rad50-HK^WT), and trimeric/tretrameric (P3) species.

Structural analyses of the complex suggest a model in which the Mre11 complex's effect on DSB repair is attributable to its ability to bridge DNA molecules in *trans* and in *cis* (de Jager et al. 2001, 2004; van Noort et al. 2003; Moreno-Herrero et al. 2005). In *trans*, two complexes bind DNA independently by their globular domains and, via association through the Rad50 hook domain, would bridge sister chromatids and promote HDR between them. Indeed, studies in yeast have shown that the dimerization function of the hook domain underlies the influence of this domain on DSB repair, telomere maintenance, and meiotic DSB formation (Wiltzius et al. 2005). In *cis*, the globular domain could bridge two DNA ends in a manner that would promote NHEJ (Williams et al. 2008). In this mode, end-to-end DNA bridging is effected by adjacent monomeric components of the dimeric globular domain (Lammens et al. 2011; Lim et al. 2011).

Mutations that target the invariant cysteines of the Rad50 hook domain (Hopfner et al. 2002; Wiltzius et al. 2005; Hohl et al. 2011; He et al. 2012) globally disrupt Mre11 complex functions and thus phenocopy the null *Rad50* mutation. Hence, the specific contribution of the Rad50 hook to the repair and signaling functions of the Mre11 complex has not been examined in isolation from the other domains of the complex.

To gain insight into Rad50 hook domain's role, our laboratory targeted the residues adjacent to the invariant cysteine residues in *S. cerevisiae* in an effort to obtain hypomorphic alleles. The alleles obtained were examined and found to encode hook domains with reduced Zn^{2+}-dependent dimerization and increased DNA damage sensitivity (M Hohl, C Tous, T Kochańczyk, A Krężel,

A Aguilera, and JHJ Petrini, in prep.). In this study, two of the yeast alleles (*rad50-46* and *rad50-47*) were modeled in mice.

We found that in the absence of the wild-type Rad50 protein, both *Rad50^46* and *Rad50^47* alleles failed to support viability at either the cellular or organismal level, consistent with the view that the Rad50 hook domain is integral to the functions of the Mre11 complex. The *Rad50^46* and *Rad50^47* gene products exerted dominant gains of function in the presence of the wild-type protein.

Heterozygous *Rad50^{+/46}* and *Rad50^{+/47}* cells were relatively proficient in DNA repair but exhibited chronic DDR signaling at the cellular level and severe ATM-dependent phenotypes at the organismal level. The data suggest that the *Rad50^46* and *Rad50^47* proteins promote aberrant heterotypic dimerization at the hook domain interface. As the functional defect imparted by *Rad50^46* and *Rad50^47* predominantly affected Mre11 complex-dependent DDR signaling, these data reveal a previously unrecognized influence of the Rad50 hook domain on Mre11 complex-dependent regulation of the apical DDR kinases.

Results

Rad50 hook domain mutants

Having previously shown that alteration of the cysteine residues of the Rad50 hook domain was tantamount to complete elimination of the protein (Hopfner et al. 2002), we reasoned that alteration of adjacent residues might result in a partial loss of function that would provide

insight regarding the functional importance of the Rad50 hook. Using *S. cerevisiae*, we identified two mutants, designated *rad50-46* and *rad50-47*, that behaved as hook domain hypomorphs and have in common the presence of charged residues in the vicinity of the cysteines that coordinate zinc (Fig. 1A). As a consequence, both mutants showed reduced hook-mediated dimerization and reduced affinity for Zn^{2+} (M Hohl, C Tous, T Kochańczyk, A Krężel, A Aguilera, and JHJ Petrini, in prep.).

A 22.7-kDa fragment of bacterially produced mouse Rad50 (Rad50-HK) that contained the hook domain flanked by small segments of the coiled-coil region was purified and examined by size exclusion chromatography and multi-angle light scattering (SEC-MALS). Rad50-HK^{WT} eluted as a single peak (Fig. 1B,C) with a molecular weight of 44.6 kDa, indicating a dimeric species. Inductively coupled mass spectrometry (ICP-MS) revealed that the protein to Zn^{2+} molar ratio of this species was 2.4, approximating the expected value of 2 for a Zn^{2+}-dependent dimer (Fig. 1D). In contrast, Rad50-HK^{46} eluted in three peaks (Fig. 1B). Peak 2 (P2) was similar to Rad50-HK^{WT} in molecular weight and Zn^{2+} content. Peak 1 (P1) and peak 3 (P3) contained very little Zn^{2+} and represent monomers and higher-molecular-weight aggregates, respectively (Fig. 1D). These data suggest that the Rad50^{46} hook domain is structurally compromised but retains some ability to dimerize and bind Zn^{2+}.

Derivation of Rad50^{46} and Rad50^{47} mice

To analyze the function of the Rad50 hook in vivo, mice expressing analogs of the yeast *rad50-46* and *rad50-47* alleles were derived. The mice initially retained a *LoxP*-flanked *neo* cassette within intron 13 of the mutant *Rad50* locus (Supplemental Fig. S1A,B). These alleles were designated *Rad50$^{+/Neo46}$* and *Rad50$^{+/Neo47}$*. *Rad50$^{+/Neo47}$* chimeric mice were unable to produce viable offspring. No live *Rad50$^{+/Neo47}$* births were noted among 327 pups produced from 27 different chimeras. PCR genotyping of tissues from *Rad50$^{+/Neo47}$* chimeras (including isolated sperm) indicated that the *Rad50^{Neo47}* allele was present (Supplemental Fig. S1C). On this basis, we concluded that the *Rad50^{Neo47}* allele exerted a dominant lethal effect. In contrast, *Rad50$^{+/Neo46}$* chimeric mice transmitted the *Rad50^{Neo46}* allele to viable offspring, and 50% of the embryonic stem cell-derived pups were *Rad50$^{+/Neo46}$*.

Rad50^{Neo46} also exerted a dominant phenotype. The effects observed were more pronounced following deletion of the *LoxP*-flanked *neo* cassette (henceforth *Rad50$^{+/46}$* mice) by crossing to *CAG-Cre* mice. *Rad50$^{+/46}$* mice were born at the expected Mendelian ratios but displayed intense skin hyperpigmentation (Fig. 2A), and 27% of them developed hydrocephalus compared with 4% of *Rad50$^{+/Neo46}$* (Fig. 2B). RT–PCR analysis indicated that the expression of *Rad50^{Neo46}* was lower than *Rad50^{46}* (Supplemental Fig. S1D). Hence, the extent of dominance was correlated with the dosage of the *Rad50^{46}* gene product.

Rad50$^{+/46}$ males were infertile (discussed further below). This precluded interbreeding of heterozygotes to obtain *Rad50$^{46/46}$* mice. Instead, *Rad50$^{+/46}$* females were crossed with *Rad50$^{\Delta/+}$* males (Luo et al. 1999). No *Rad50$^{46/\Delta}$* mice were obtained from 90 offspring (χ^2, $P < 10^{-4}$), indicating that the *Rad50^{46}* allele does not support embryonic viability.

Rad50$^{+/46}$ and *Rad50$^{+/\Delta}$* mice were crossed with *Rad50$^{ind/ind}$* (in which exons 1 and 2 are flanked by *loxP* sites) (Adelman et al. 2009) and a tamoxifen-inducible *Cre* (Ventura et al. 2007). In this setting, Cre-mediated excision of the floxed exons of the *Rad50^{ind}* allele to generate *Rad50$^{46/-}$* and *Rad50$^{\Delta/-}$* cells in vivo was carried out. The induction of *Cre* is variable in vivo, and so affected tissues were likely to exhibit mosaicism for the deletion genotype. Tamoxifen administered in the food produced excision in the *Rad50^{ind}* allele in various tissues but was predominant in the intestine (Supplemental Fig. S2B). *Rad50$^{46/-}$* and *Rad50$^{\Delta/-}$* mosaic mice did not live beyond 2 wk due to intestinal failure. Histological analysis of the gut 9 d after beginning the treatment evidenced a profound alteration of *Rad50$^{46/-}$* intestinal morphology (Supplemental Fig. S2C). These data indicate that the *Rad50^{46}* allele does not support the viability of proliferating cells in vivo.

DNA repair and checkpoint signaling in Rad50$^{+/46}$ cells

We sought to determine the molecular basis of the *Rad50$^{+/46}$* phenotype. SV40-immortalized *Rad50$^{+/46}$* and *Rad50$^{+/+}$* mouse embryonic fibroblasts (MEFs) showed similar levels of Mre11 complex proteins, and immunoprecipitations indicated that complex integrity was not overtly compromised (Fig. 2C).

The DNA repair functions of the Mre11 complex were modestly affected in *Rad50$^{+/46}$* cells. *Rad50$^{+/46}$* cells showed increased sensitivity to camptothecin at high doses (Fig. 2D) but were not sensitive to other DNA-damaging agents (Supplemental Fig. S3A). Accordingly, treatment with clastogens failed to increase the yield of chromosomal aberrations relative to wild-type cells (Supplemental Fig. S3B). The DR-GFP assay, in which an I-SceI/GFP reporter is integrated at the *Pim1* locus (Kass et al. 2013), was employed to assess HDR proficiency. An I-SceI-IRES-hCD4 retroviral vector, which allowed cell sorting of I-SceI-expressing cells, was used to minimize the confounding effects of poor transfectability and varying transfection efficiencies of the cells examined. We found that *Rad50$^{+/46}$* cells consistently exhibited a trend of lower HDR efficiency, although the difference was not statistically significant ($P = 0.17$) (Fig. 2E).

The Mre11 complex is required for ATM activation (Stracker and Petrini 2011). *Rad50$^{+/46}$* cells exhibited indices of spontaneous ATM activation, including pS1987-ATM and γH2AX formation (Fig. 2F). IR-induced ATM activation in *Rad50$^{+/46}$* cells was otherwise normal and occurred with wild-type kinetics (Fig. 2F). *Rad50$^{+/47}$* skin fibroblasts generated from chimeric mice phenocopied *Rad50$^{+/46}$* cells in all respects (Supplemental Fig. S4). These results suggested that *Rad50$^{+/46}$* (and *Rad50$^{+/47}$*) cells exhibited spontaneous DNA damage. An alternative nonexclusive possibility is that the *Rad50^{46}* and *Rad50^{47}* alleles are hypermorphic with respect to DNA damage
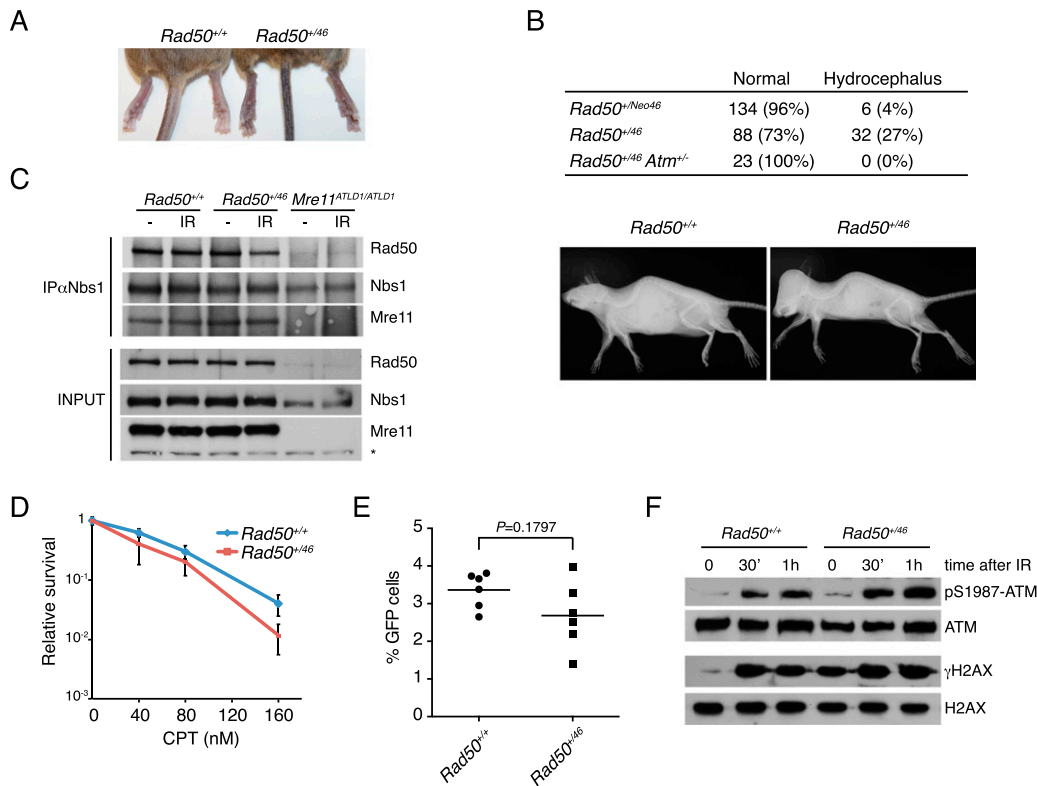
Figure 2. *Rad50^46* allele is dominant. (*A*) Representative image showing hyperpigmentation in tail and paws in a *Rad50^{+/46}* mouse compared with a *Rad50^{+/+}* littermate. (*B*) Incidence of hydrocephalus in *Rad50^{+/46}*, *Rad50^{+/Neo46}*, and *Rad50^{+/46} Atm^{+/−}* mice and representative X-ray images of an 8-wk-old *Rad50^{+/46}* mouse with hydrocephalus and a *Rad50^{+/+}* littermate. (*C*) Rad50, Mre11, and Nbs1 protein levels in *Rad50^{+/+}* and *Rad50^{+/46}* SV40-immortalized MEFs and Nbs1 immunoprecipitation to assess Mre11 complex integrity in mock-treated cells (−) or 1 h after 5 Gy IR. *Mre11^{ATLD1/ATLD1}* cells were used as control for cells with reduced Mre11 complex levels (Theunissen et al. 2003). (*D*) SV40-immortalized MEFs were treated with camptothecin for 24 h, and colonies were assessed 10 d later. Experiments were done three times in triplicate using two independent cell lines per genotype. Error bars depict standard deviation (SD). (*E*) Primary mouse fibroblasts *Rad50^{+/+} Pim1^{+/DR-GFP}* and *Rad50^{+/46} Pim1^{+/DR-GFP}* were infected with SceI-IRES-hCD4 retrovirus, and GFP^+ cells were assessed 72 h after infection. The efficiency of GFP^+ is measured relative to the infected-only (CD4^+) cells. Experiments were done in triplicate with two independent cell lines per genotype. *P*-value was determined by Wilcoxon rank-sum test. (*F*) SV40-immortalized MEFs of the indicated genotypes were left untreated (*t* = 0) or irradiated with 2 Gy IR, and the levels of pS1987-ATM and γH2AX were assessed in the indicated time points.

signaling, as observed previously in *Rad50^{S/S}* mice (and yeast) (Usui et al. 2006), and thereby exhibited indices of ATM activation at levels disproportional to the extent of DNA damage. This latter interpretation predicts that *Rad50^{46}* phenotypes would be ATM-dependent.

The Rad50^{+/46} phenotype is ATM-dependent

Precedent for the hypothesis that *Rad50^{+/46}* phenotypes could be ATM-dependent comes from *Rad50^{S/S}* mice, which at both the cellular and organismal levels exhibited phenotypes reminiscent of *Rad50^{+/46}* (Bender et al. 2002; Morales et al. 2005). We found that most aspects of the *Rad50^{+/46}* pathology, including hydrocephalus (Fig. 2B), were rescued in the context of *Atm* heterozygosity, demonstrating the acute ATM dependence of the *Rad50^{+/46}* phenotype.

Mre11 complex-dependent ATM signaling affects the viability and proliferative behavior of Lin^− Sca1^+ c-Kit^+ (LSK) cells, which contain primitive hematopoietic compo-

nents, including hematopoietic stem cells (HSCs) and lineage progenitors (Morales et al. 2008). *Rad50^{+/46}* mice showed an altered LSK population characterized by an expansion (average increase of 4.7-fold) of the multipotent precursors (MPPs) (Fig. 3A). This phenotype was also dependent on ATM because it was suppressed in *Rad50^{+/46} Atm^{+/−}* mice (Fig. 3A). The increased MPP population was not correlated with elevated levels of its proximal descendants, the common lymphoid progenitor (CLP) and common myeloid progenitors (CMPs) (Fig. 3B). CFU-S assays, which measure the ability of MPPs to differentiate and form colonies in the spleen of lethally irradiated mice, were carried out (Spangrude et al. 1988). We noted a 50% reduction in the colony-forming ability of *Rad50^{+/46}* MPP cells (Fig. 3C). These data indicate that the expanded *Rad50^{+/46}* MPP population is not fully functional.

A remarkable outcome in *Rad50^{S/S} Atm^{−/−}* mice was the suppression of lymphomagenesis associated to ATM deficiency (Morales et al. 2005; Usui et al. 2006). Similarly, the latency of thymic lymphomas typical of the
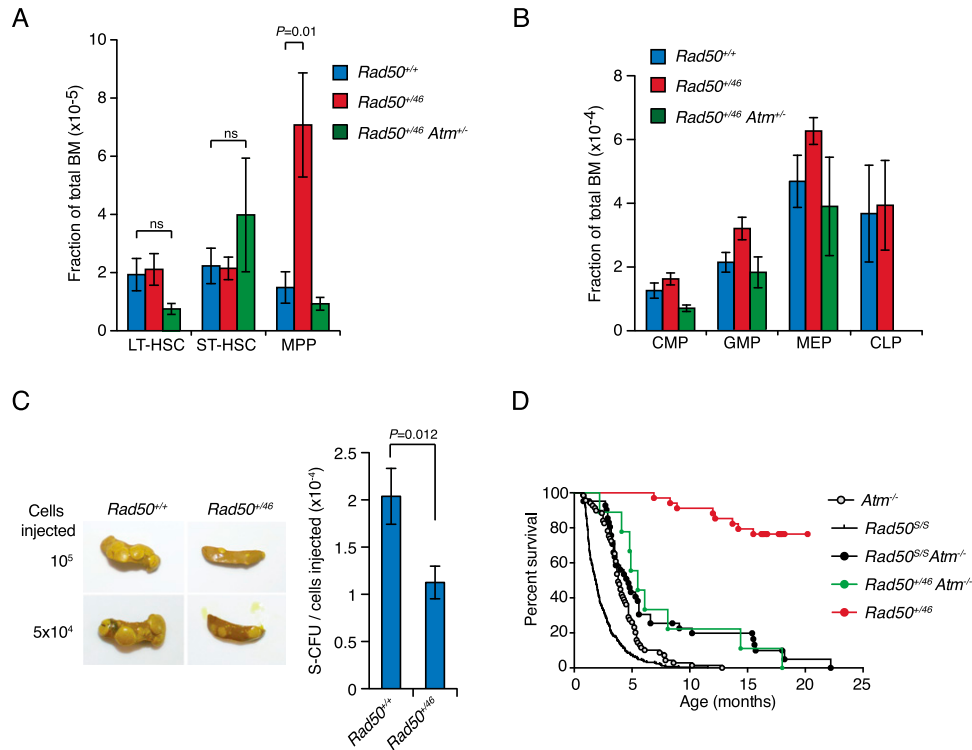
Figure 3. ATM-dependent hematopoietic alterations in $Rad50^{+/46}$ mice. (*A*) Quantification of long-term hematopoietic stem cells (LT-HSC), short-term hematopoietic stem cells (ST-HSC), and MPPs in bone marrow from mice of the indicated genotypes. Bars denote the average ± standard error of mean (SEM). $Rad50^{+/+}$, n = 8; $Rad50^{+/46}$, n = 8,; $Rad50^{+/46}$ $Atm^{+/−}$, n = 2. (*B*) Quantification of CMP, granulocyte macrophage progenitor (GMP), megakaryocyte erythroid progenitor (MEP), and CLP. Bars denote the average ± SEM. $Rad50^{+/+}$, n = 5; $Rad50^{+/46}$, n = 5; $Rad50^{+/46}$ $Atm^{+/−}$, n = 2. *P*-values were determined by unpaired *t*-test. (*C*) Representative images and quantification of CFU-S assay at day 13 using bone marrow cells of the indicated genotype. Bars denote the average ± SEM of all the spleens obtained from three independent experiments. $Rad50^{+/+}$, n = 21; $Rad50^{+/46}$, n = 20; $Rad50^{+/46}$ $Atm^{+/−}$, n = 5. *P*-values were determined by unpaired *t*-test. (*D*) Kaplan-Meier survival curves of $Atm^{−/−}$, $Rad50^{S/S}$, $Rad50^{S/S}$ $Atm^{−/−}$ (previously published; Morales et al. 2005), $Rad50^{+/46}$, and $Rad50^{+/46}$ $Atm^{−/−}$ mice. $Rad50^{+/46}$ mouse survival was not assessed beyond 18 mo, and thus the events were censored at that age.

$Atm^{−/−}$ genoytpe was markedly increased in $Rad50^{+/46}$ $Atm^{−/−}$ mice (Fig. 3D). In light of recent data suggesting a role for the Mre11 complex in ATR activation (Duursma et al. 2013; Shiotani et al. 2013), the suppression of lymphomagenesis in $Rad50^{+/46}$ $Atm^{−/−}$ mice may reflect compensatory Mre11 complex-dependent ATR activation.

Germ cell dysfunction in Rad50$^{+/46}$ mice

$Rad50^{+/46}$ mice exhibited severe fertility defects. All males and 27% of the females were infertile, and the remaining $Rad50^{+/46}$ females produced fewer and smaller litters than $Rad50^{+/+}$ controls during the same breeding period (Supplemental Fig. S5A,B). $Rad50^{+/46}$ exhibited ovarian and testicular atrophy (Fig. 4A,B), and the seminiferous tubules displayed severely reduced cellularity (Fig. 4C). As with the hematopoietic phenotype, testicular defects were ATM-dependent. Testes from $Rad50^{+/46}$ $Atm^{+/−}$ mice were twofold larger than those from $Rad50^{+/46}$ (Fig. 4A), and the cellularity of the seminiferous tubules was increased (Fig. 4C).

Immunohistochemical staining for the synaptonemal complex protein SYCP3 revealed that $Rad50^{+/46}$ mice showed an eightfold reduction in meiotic prophase cells per tubule (Fig. 4C,D). Similar analyses revealed a 23-fold reduction in SYCP3-positive cells from 14-dpp $Rad50^{+/46}$ mice (Supplemental Fig. S5C,D). TUNEL staining of $Rad50^{+/46}$ tubules from adult and juvenile mice was unremarkable (Fig. 4C,D; Supplemental Fig. S5C,D), suggesting that the reduction in $Rad50^{+/46}$ meiotic cells was not due to apoptotic attrition. The reduction in cellularity did not appear to reflect a stage-specific block in meiotic progression, as chromosome spreads from the rare meiotic cells present revealed spermatocytes in all stages of meiosis (Supplemental Fig. S5E).

Spo11 protein initiates meiotic recombination by forming DSBs through a covalent protein–DNA intermediate. Spo11 is cleaved from DSB ends to liberate Spo11–oligonucleotide complexes (Neale et al. 2005) by a process that in yeast requires activity of the Mre11 complex (Neale et al. 2005; Milman et al. 2009). In *S. cerevisiae rad50-46* mutants, DSBs are formed, but Spo11 remains covalently bound to genomic DNA (M Hohl, C Tous, T Kochańczyk, A Krężel, A Aguilera, and JHJ Petrini, in prep.). We tested whether a defect in removal of Spo11 from DSB ends accounted for the infertility of $Rad50^{+/46}$
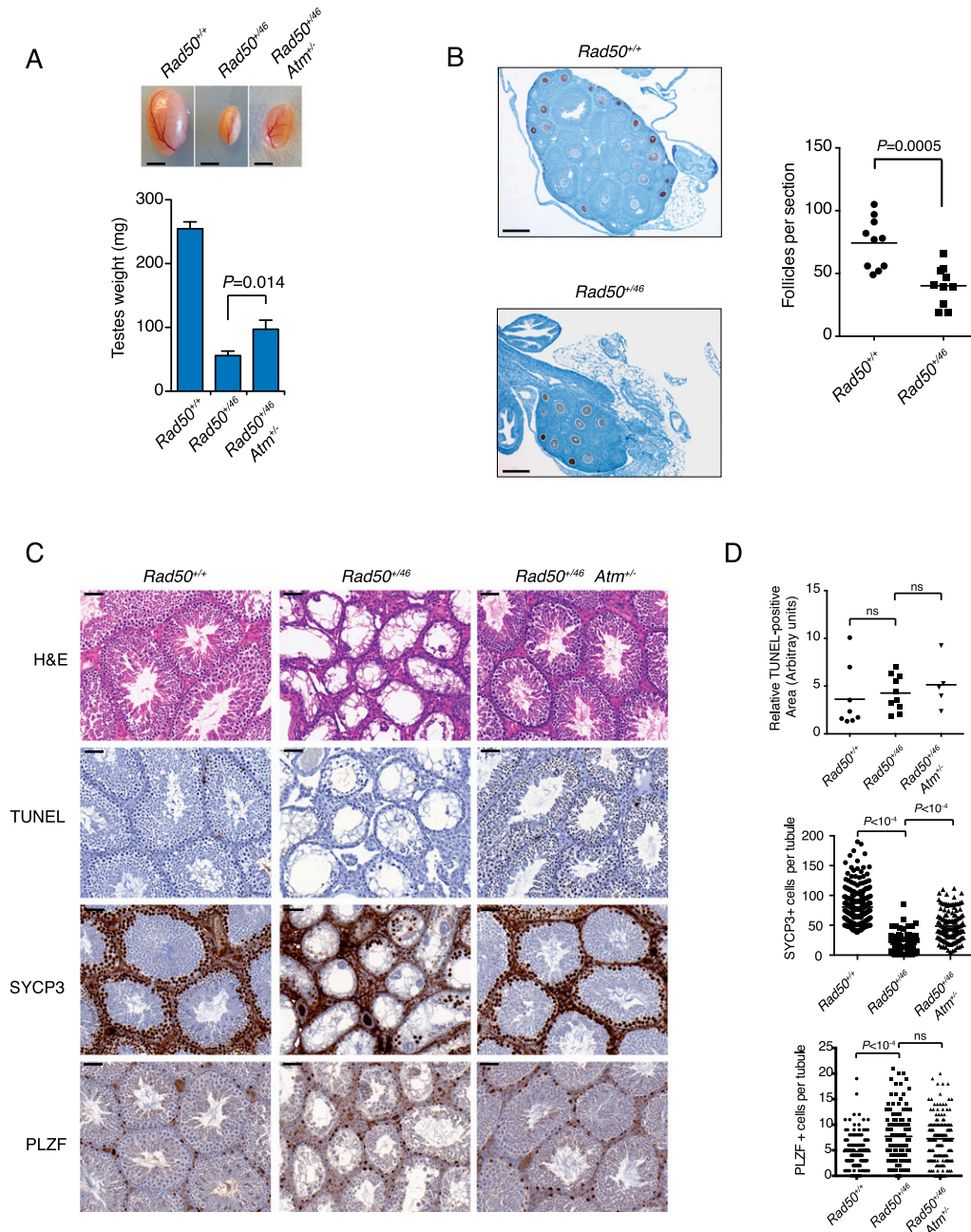
Figure 4. Germ cell dysfunction in $Rad50^{+/46}$ mice. (*A*) Representative images of testis from mice of the indicated genotypes and average testes weight ± SEM ($Rad50^{+/+}$, $n = 7$; $Rad50^{+/46}$, $n = 8$; $Rad50^{+/46}$, $Atm^{+/-}$ $n = 5$). Bar, 2.5 mm. (*B*) Representative images of anti-VASA-stained mid-ovary sections from 3-wk-old mice and quantification of the number follicles. Bar, 0.4 mm. Ovaries analyzed: $n = 10$. *P*-value was determined by unpaired *t*-test. (*C*) Hematoxylin and eosin (H&E), TUNEL, SYCP3, and PLZF immunohistochemical staining of testis sections from adult mice of the indicated genotypes. Bar, 50 μm. (*D*) Quantification of immunohistochemical staining from *C*. The TUNEL-positive area is expressed as a ratio to the total testis area. Testis analyzed: $Rad50^{+/+}$, $n = 8$; $Rad50^{+/46}$, $n = 10$; $Rad50^{+/46}$ $Atm^{+/-}$, $n = 5$. *P*-values were determined by unpaired *t*-test.

mice. Spo11–oligonucleotide complexes were nearly absent in adult and juvenile $Rad50^{+/46}$ mice (Supplemental Fig. S5F). The reduction in Spo11–oligonucleotide complexes in $Rad50^{+/46}$ testes was not simply a consequence of testicular atrophy because they were evident in $Dmc1^{-/-}$ testes, which, like $Rad50^{+/46}$, are severely atrophic (Supplemental Fig. S5F). These data suggested that in $Rad50^{+/46}$

mice, meiotic DSBs are not created, or Spo11 is not released following DSB formation. We could not exclude the possibility that this effect is due to the paucity of meiotic cells in $Rad50^{+/46}$ testes. To directly address whether defects in the formation or repair of meiotic DSBs were the cause of infertility of $Rad50^{+/46}$ mice, we generated $Rad50^{+/46}$ $Spo11^{-/-}$ mice. Seminiferous tu-

bules from $Rad50^{+/46}$ mice showed reduced cellularity compared with $Spo11^{-/-}$ (Supplemental Fig. S5G). Analysis of sections from $Rad50^{+/46}$ $Spo11^{-/-}$ mice revealed that $Rad50^{+/46}$ was epistatic to $Spo11^{-/-}$. This result indicated that the $Rad50^{+/46}$ phenotype was independent of $Spo11$ and thus excluded the possibility of impaired Spo11 removal as a cause of $Rad50^{+/46}$ infertility.

These data suggest that the $Rad50^{+/46}$ defect was manifest prior to initiation of the meiotic program. Supporting that interpretation, $Rad50^{+/46}$ tubules displayed 1.6-fold more cells positive for PLZF (a marker of undifferentiated spermatogonia) (Buaas et al. 2004; Costoya et al. 2004) compared with $Rad50^{+/+}$ mice (Fig. 4C,D). This expansion of primitive precursors together with the reduction of meiotic cells and the lack of increased cell death was consistent with a block in spermatogonial differentiation, analogizing the block observed in primitive hematopoietic precursors.

Mre11 complex and ATM activation in Rad50$^{46/-}$ cells

$Rad50^{46/ind}$ and $Rad50^{\Delta/ind}$ MEFs and ear fibroblast (EF) cultures were established. Lentiviral-mediated delivery of Cre resulted in excision within the $Rad50^{ind}$ allele in 3 d (Supplemental Fig. S6A) to produce $Rad50^{\Delta/-}$ and $Rad50^{46/-}$ cells that could be maintained in culture for 7–8 d after Cre infection. This provided a window of time to assess the outcome of limiting cells to Rad50^{46} as the sole source of Rad50 protein. As shown previously in $Rad50^{\Delta/-}$ cell extracts (Adelman et al. 2009), $Rad50^{46/-}$ cells displayed decreased levels of Rad50, Mre11, and Nbs1 (Fig. 5A), suggesting that Mre11 complex proteins were less stable in $Rad50^{46/-}$ cells.

Acute disruption of the Mre11 complex results in a dramatic increase in chromosomal aberrations (Demuth et al. 2004; Frappart et al. 2005; Reina-San-Martin et al. 2005; Yang et al. 2006; Adelman et al. 2009). Excision in the $Rad50^{ind}$ allele in $Rad50^{46/ind}$ cells produced a similar outcome, with 53% of $Rad50^{\Delta/-}$ and 42% of $Rad50^{46/-}$ cells showing chromosomal aberrations compared with 12% of $Rad50^{+/-}$ (Fig. 5B). Cells with multiple aberrations (three or more) were not seen in $Rad50^{+/-}$ controls but represented up to 30% and 11.8% in $Rad50^{\Delta/-}$ and $Rad50^{46/-}$, respectively (Supplemental Fig. S6B).
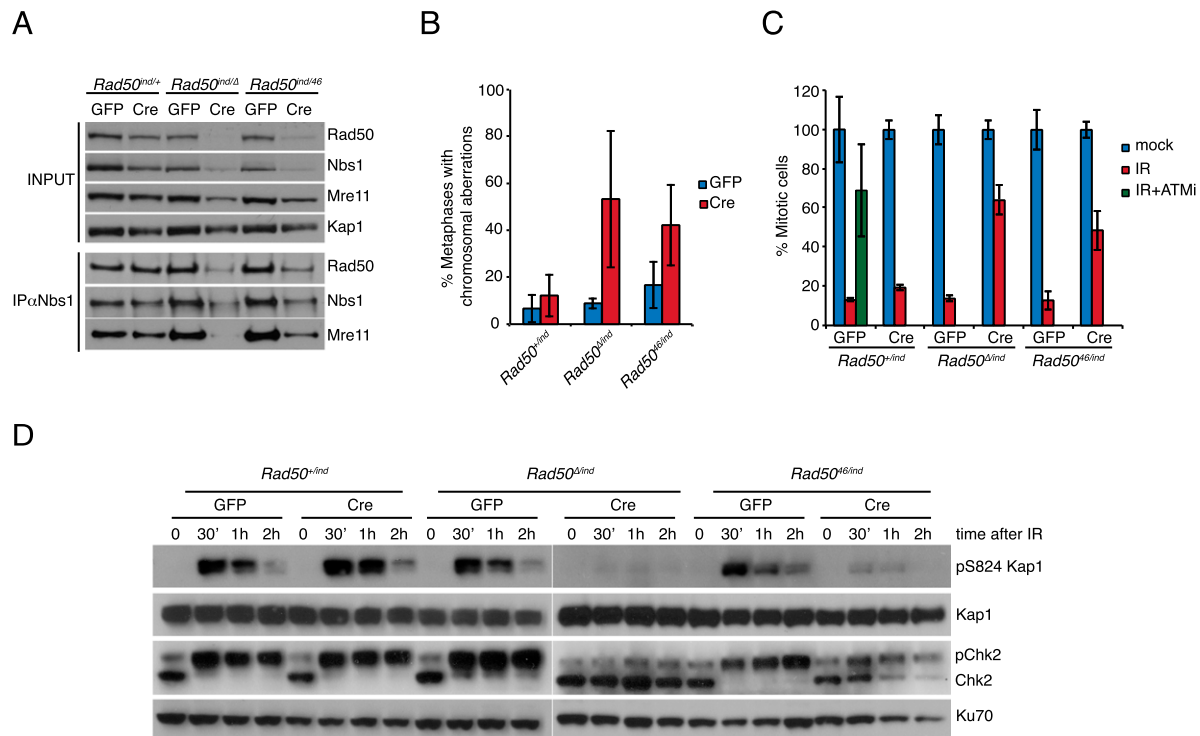

Figure 5. Mre11 complex and ATM activation in $Rad50^{46/-}$ cells. (A) Analysis of Mre11 complex levels in $Rad50^{+/ind}$, $Rad50^{\Delta/ind}$, and $Rad50^{46/ind}$ SV40-immortalized MEFs 8 d after the lentiviral delivery of Cre or GFP and Nbs1 immunoprecipitation to assess the Mre11 complex integrity in the same cells. Kap1 was used as loading control. (B) Analysis of chromosomal aberrations in $Rad50^{+/ind}$, $Rad50^{\Delta/ind}$, and $Rad50^{46/ind}$ SV40-immortalized MEFs 8 d after the lentiviral delivery of Cre or GFP. Shown is average ± SD of three independent experiments. Twenty-five or more metaphases were scored per genotype and experiment. (C) Analysis of the G2/M checkpoint in $Rad50^{+/ind}$, $Rad50^{\Delta/ind}$, and $Rad50^{46/ind}$ SV40-immortalized MEFs 8 d after the lentiviral delivery of Cre or GFP. Mitotic cells were determined in mock-treated cells or 1 h after 5 Gy IR by measuring the phospho-Ser10 Histone H3-positive cells. The ATM inhibitor KU-55933 was added 2 h before IR treatment and kept throughout the experiment. Shown is average mitotic ratio relative to mock-treated ± SD of two independent experiments done in triplicate. (D) Analysis of pS824-Kap1 and Chk2 phosphorylation in $Rad50^{+/ind}$, $Rad50^{\Delta/ind}$, and $Rad50^{46/ind}$ SV40-immortalized MEFs 8 d after the lentiviral delivery of Cre or GFP after 2 Gy of γ radiation. Time 0 corresponds to untreated cells. Note that Chk2 migrates as a higher-molecular-weight species when phosphorylated (pChk2). Ku70 levels were used as loading control.

$Rad50^{\Delta/-}$ MEFs were unable to activate ATM in response to IR, as evidenced by reduced phosphorylation of Kap1 and Chk2 following IR treatment (Fig. 5D). $Rad50^{46/-}$ MEFs were also impaired in ATM activation but to a lesser extent. Whereas phosphorylation of Kap1 and Chk2 was undetectable in $Rad50^{\Delta/-}$ MEFs, we could consistently detect it in $Rad50^{46/-}$ MEFs (Fig. 5D). This suggests that $Rad50^{46/-}$ cells retain a degree of Mre11 complex function; however, this observation may reflect the presence of residual wild-type Rad50 protein.

Reduced ATM activation in $Rad50^{46/-}$ cultures was associated with impairment of the DNA damage-dependent G2/M checkpoint. One hour after 5 Gy of IR, cells with at least one copy of wild-type $Rad50$ showed an 80%–90% reduction in the mitotic cells, indicative of a proficient G2/M checkpoint (Fig. 5C). Excision in the $Rad50^{ind}$ allele to produce $Rad50^{\Delta/-}$ or $Rad50^{46/-}$ cells caused defects in the G2/M checkpoint, with cells exhibiting only a 36% and 52% reduction in the proportion of mitotic cells, respectively, after IR (Fig. 5C).

Rad50[46] promotes tumorigenesis

The Mre11 complex has been implicated in the suppression of malignancy in several contexts (Stracker and Petrini 2011; Foster et al. 2012; Gupta et al. 2013). Accordingly, cohorts of 30 $Rad50^{+/46}$, 31 $Rad50^{+/Neo46}$, and 34 $Rad50^{+/+}$ mice were followed for 18 mo. Although no signs of morbidity were evident, multiple liver neoplasms were noted upon necropsy. The incidence was 26% in $Rad50^{+/Neo46}$ mice, 37% in $Rad50^{+/46}$ mice, and 3% in $Rad50^{+/+}$ mice (Fig. 6A). Most of the affected mice presented hyperplastic nodules and/or adenomas, but 10% of $Rad50^{+/46}$ mice developed malignant hepatoblas-

toma (Fig. 6A,B). Unlike adenomas, which arise from mature hepatocytes, hepatoblastomas arise from hepatic progenitor cells of the portal areas (Marquardt and Thorgeirsson 2010). This indicates that both differentiated hepatocytes and immature progenitors are susceptible to $Rad50^{46}$-induced malignancy.

Discussion

We showed previously that alteration of either invariant cysteine of the *S. cerevisiae* Rad50 hook domain results in complete inactivation of Rad50, limiting the ability to distinguish hook-specific from general Mre11 complex functions (Hopfner et al. 2002). The residues between the cysteines are also nearly invariant. The first is either Pro (85%) or Tyr (10%), and the second position contains Leu or Val in 80% of the cases (Stracker and Petrini 2011). In this study, the functional significance of the Rad50 hook domain in the mammalian Mre11 complex was examined through the generation of mouse mutants affecting those residues. Neither of the hook mutants encoded gene products that support viability at the organismal or cellular level, indicating that, as in *S. cerevisiae*, the hook domain is required for Mre11 complex function in mammals. In the heterozygous configuration, we found that $Rad50^{46}$ and $Rad50^{47}$ behaved as dominant gain-of-function alleles that promoted chronic DDR signaling. These outcomes at the molecular level were associated with severe phenotypes in vivo, including embryonic lethality, hydrocephalus, defects in the development and maintenance of primitive cells of the bone marrow and germline, and increased incidence of liver neoplasms.

Rad50[46] is not a loss-of-function allele

Despite the phenotypic severity observed, the data are inconsistent with $Rad50^{46}$ being a null allele. First, the phenotypes in $Rad50^{46/-}$ cells are milder than $Rad50^{\Delta/-}$. Although perdurance of wild-type Rad50 protein following *Cre*-mediated deletion in $Rad50^{46/ind}$ cultures cannot be excluded, $Rad50^{46}$ may retain limited functionality. Second, $Rad50^{46}$ exerts dose-dependent dominance; the phenotype of $Rad50^{+/Neo46}$, in which expression of the mutant gene is lower than in $Rad50^{+/46}$, was less severe. In contrast, $Rad50^{+/\Delta}$ mice and cells are indistinguishable from wild-type (CF Bender, CA Adelman, and JHJ Petrini, unpubl.). Hence, the observed phenotypes do not simply reflect reduced dosage of wild-type $Rad50$. Finally, genetic ablation of $Rad50$ in the liver is not associated with detectable pathology (Adelman et al. 2009), whereas liver neoplasia and liver tumors were common in $Rad50^{+/46}$ mice.

Given that mutations in $Rad50^{46}$ and $Rad50^{47}$ affect one of the Mre11 complex's dimerization domains, it is likely that the dominant behavior of these alleles results from interaction of the mutant gene product with the wild-type Rad50 protein. Supporting this hypothesis, we found that Rad50[WT] and Rad50[46] hook domains interact in vitro (Supplemental Fig. S7). In principle, $Rad50^{+/46}$
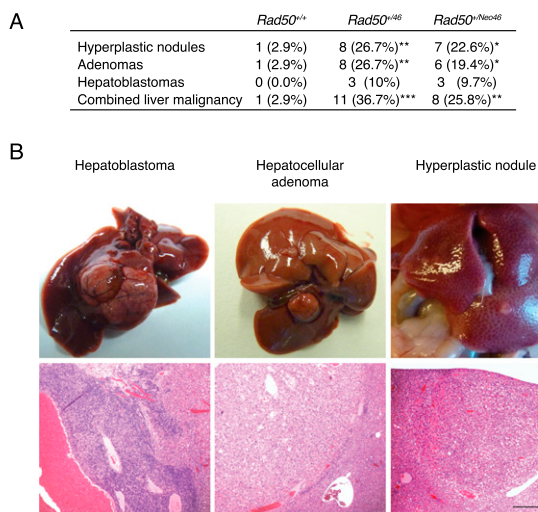
	$Rad50^{+/+}$	$Rad50^{+/46}$	$Rad50^{+/Neo46}$
Hyperplastic nodules	1 (2.9%)	8 (26.7%)**	7 (22.6%)*
Adenomas	1 (2.9%)	8 (26.7%)**	6 (19.4%)*
Hepatoblastomas	0 (0.0%)	3 (10%)	3 (9.7%)
Combined liver malignancy	1 (2.9%)	11 (36.7%)***	8 (25.8%)**

Figure 6. $Rad50^{+/46}$ and $Rad50^{+/Neo46}$ mice develop liver tumors. (A) Frequency of liver tumors developed by $Rad50^{+/+}$, $Rad50^{+/46}$, and $Rad50^{+/Neo46}$ mice by 18 mo of age. *P*-values were calculated with Fisher's exact test comparing with $Rad50^{+/+}$. (*) $P \leq 0.05$; (**) $P \leq 0.01$; (***) $P \leq 0.001$. (B) Representative images and H&E staining of the hepatic tumors developed by $Rad50^{+/46}$ and $Rad50^{+/Neo46}$ mice. Bar, 200 μm for all images.

cells could contain wild-type homodimers, mutant/wild-type heterodimers, and mutant homodimers. The $Rad50^{+/46}$ phenotypes observed are likely attributable to heterotypic complexes. Several lines of evidence indicate that alterations of the hook domain exert global effects on Mre11 complex function (Hopfner et al. 2002; Wiltzius et al. 2005; Hohl et al. 2011). The data presented here further suggest that these effects can be exerted in *trans* within the dimeric assembly of the complex.

Chronic DDR signaling

$Rad50^{+/46}$ and $Rad50^{+/47}$ cells exhibit constitutive γH2AX formation. However, $Rad50^{+/46}$ cells exhibited only a modest reduction in HDR efficiency and a slight sensitivity to camptothecin and did not show increased spontaneous chromosomal aberrations. These facts are inconsistent with spontaneous DNA damage as the cause of γH2AX formation and suggest the possibility that $Rad50^{+/46}$ behaves as a hypermorph with respect to DNA damage signaling, as previously observed for the $Rad50S$ allele (Usui et al. 2006). Although the underlying mechanisms of Mre11 complex-dependent DDR regulation remain unclear, the increased latency of lymphomas in $Rad50^{+/46}$ $Atm^{-/-}$ mice supports this interpretation.

The $Rad50^S$ and $Rad50^{46}$ mutations affect domains widely separated yet engender similar DDR signaling phenotypes ($Rad50^S$ is the K20M substitution). AFM studies have shown that DNA binding by the globular domain promotes spatial reorganization of the coiled-coil and hook domain (Moreno-Herrero et al. 2005). Conversely, $Rad50^{+/46}$ and $Rad50^{+/47}$ mutations as well as mutations that truncate the Rad50 coiled-coil domain affect functions that are likely specified within the globular domain (Hohl et al. 2011). These data illustrate the functional interdependence of the hook and globular domains within the Mre11 complex.

The $Rad50^{+/46}$ phenotype and progenitor cells

Consistent with the interpretation that the $Rad50^{46}$ allele chronically activates ATM, the phenotypic outcomes in $Rad50^{+/46}$ mice are dependent on *Atm*. Again, this situation is comparable with $Rad50^{S/S}$ mice, and the tissues primarily affected are the same: primitive cells in the hematopoietic and germline lineages. These observations indicate that the Mre11–ATM-dependent signaling pathway is important for the maintenance and function of primitive cells in the bone marrow and germline (Morales et al. 2008; Takubo et al. 2008; Maryanovich et al. 2012). The Mre11 complex–ATM signaling axis likely affects progenitor cells in other organs systems (Shiloh and Ziv 2013). For example, hyperpigmentation, common to both $Rad50^{S/S}$ and $Rad50^{+/46}$, has also been observed in mice with chronic DDR signaling in the skin due to telomere dysfunction (Hockemeyer et al. 2008; He et al. 2009; Martinez et al. 2010) or DNA repair defects (Zhang et al. 2011). In those instances, melanocyte expansion appears to occur in response to epidermal stem cell depletion (Stout and Blasco 2009).

Tumorigenesis in Rad50$^{+/46}$ mice

Roughly a quarter (26.7%) of $Rad50^{+/46}$ mice developed hepatocellular adenomas that were frequently coincident with additional preneoplastic lesions, primarily hyperplastic nodules and areas of disorganized architecture. The Mre11 complex–ATM pathway has been previously implicated in liver cancer, as *Atm* is required for diethylnitrosamine-induced liver carcinogenesis (Teoh et al. 2010). Notably, almost one-third of the tumor-bearing mice developed hepatoblastoma, a rare tumor that in humans primarily affects infants and children. The blastic and undifferentiated character of this tumor suggests that it arises from hepatic progenitor cells of the portal areas (Marquardt and Thorgeirsson 2010). This outcome represents an additional instance in which Mre11 complex–ATM signaling affects homeostasis by affecting progenitor cells.

Mre11 complex mutations have been identified in ~4% of human tumors (data from cBioPortal; Cerami et al. 2012). The observation here of dominant *Rad50* mutations promoting tumorigenesis supports the possibility that heterozygous Mre11 complex mutations may underlie tumor development, a possibility that should be considered in the genomic analysis of tumors.

Materials and methods

Rad50-HK expression, purification, and analysis

6xHis-SMT3-tagged Rad50-HK proteins (amino acids 591–773) were expressed in *Escherichia coli*. Soluble extracts were prepared in HK buffer (200 mM NaCl, 50 mM Tris at pH 7.5, 0.2% NP-40, 10% glycerol, 0.5 mM DTT) plus protease and phosphatase inhibitors and was purified by nickel-chelating affinity chromatography followed by Ulp1 protease treatment and a second nickel-chelating affinity purification step to separate the 6xHis-SMT3 tag. Rad50-HK proteins were analyzed by SEC using a 24-mL Superdex200 column equilibrated with 20 mM Tris (pH 7.6), 500 mM NaCl, 0.1 mM EDTA, and 2 mM DTT.

SEC-MALS was performed as described (Rambo and Tainer 2010) with a size exclusion column equilibrated with 20 mM Tris (pH 7.6), 500 mM NaCl, 0.1 mM EDTA, and 1 mM tris(2-carboxyethyl)phosphine. MALS experiments were performed using an 18-angle DAWN HELEOS light-scattering detector connected in tandem to an Optilab refractive index concentration detector (Wyatt Technology). Metal concentrations were measured using a quadrupole-based ICP-MS (7500ce, Agilent Technologies) equipped with a MicroMist nebulizer (Agilent Technologies).

Gene targeting and mice

The targeting vectors were constructed using the recombineering method previously described (Liu et al. 2003). Targeting was carried out via electroporation into the embryonic stem cell AC1 that had a 129/SvEv-background (gift of G. Oltz and E. Rhuley). Selection, clonal expansion, and analysis were performed using previously published procedures (Luo et al. 1999). Chimeras were generated at the SKI Transgenic Facility using standard methods, and male chimeras were crossed with C57BL6 mice to detect germline transmission. $Rad50^{+/Neo46}$ mice were mated with *CAG-Cre* transgenic mice (Sakai and Miyazaki 1997) to generate

the *Rad50⁴⁶* allele. All mice were maintained on mixed 129/SvEv and C57BL6 background.

Mice were housed in ventilated rack caging in a pathogen-free facility. The Institutional Animal Care and Use Committee of Memorial Sloan-Kettering Cancer Center approved animal use protocols. $Atm^{-/-}$ and $Spo11^{-/-}$ mice were previously described (Barlow et al. 1996; Baudat et al. 2000).

Cellular assays

MEFs and EFs were generated, cultured, and immortalized as described (Bender et al. 2002). $Rad50^{+/47}$ EFs were generated from $Rad50^{+/Neo47}$ chimeric mice by growing the cells in medium containing 1 mg/mL G418 followed by lentiviral delivery of *Cre* and clonal selection.

Western blots were carried out on 40 μg of protein extracted with NTEN (20 mM Tris at pH 8, 150 mM NaCl, 1 mM EDTA, 0.5% NP-40) plus protease and phosphatase inhibitors. For H2AX blots, we used 3 μg of the histone fraction extracted with 0.1 M HCl after a pre-extraction with NTEN. All of the antibodies were incubated overnight at 4°C in 5% milk. The antibodies used were rabbit anti-Rad50 polyclonal (custom Petrini laboratory antibody m84-7), rabbit anti-Nbs1 polyclonal (custom Petrini laboratory antibody 92-5), rabbit anti-Mre11 polyclonal (custom Petrini laboratory antibody 42-5), ATM (Cell Signaling), ATM pS1981 (Cell Signaling), γH2AX (Millipore), H2AX (Bethyl Laboratories), Kap1 pS824 (Abcam), Kap1 (Novus Biologicals), Chk2 (Clone 7, Millipore), and Ku70 (Santa Cruz Biotechnology).

For Nbs1 immunoprecipitation, cell extracts of SV40-immortalized MEFs were prepared with lysis buffer A (300 mM NaCl, 20 mM Tris at pH 8.0, 0.5% sodium deoxicholate, 1% Triton X-100, 5 mM MgCl₂ supplemented with protease and phosphatase inhibitors). Total protein (0.5 mg) was incubated with 2 μL of anti-Nbs1 antisera and protein A-agarose beads (Amersham) for 3 h at 4°C, washed extensively, and eluted with Laemmli's buffer.

For colony-forming assays, cells were treated with the indicated clastogens and plated in triplicate, and colonies were assessed 10 d later by staining with crystal violet.

Metaphases were prepared from cultures treated with 2×10^{-7} M colcemid for 1 h. Cells were harvested, hypotonically swelled with 0.075 M KCl for 15 min at 37°C, fixed, washed in ice-cold 3:1 methanol:acetic acid, and dropped on slides. Slides were stained with 5% Giemsa (Sigma) for 10 min and rinsed with distilled water, and coverslips were mounted with Permount (Fisher). Images were captured using an Olympus IX60 microscope and imaged with a Hammamatsu CCD camera. More than 25 spreads were scored for each sample.

G2/M checkpoint was done as previously described (Theunissen and Petrini 2006).

Lentiviral production, concentration, and titering were carried out using previously described methods (Dull et al. 1998; Lois et al. 2002). For lentivirus-*Cre* and lentivirus-*GFP* infections, 5×10^4 cells were resuspended in 3 mL of DMEM supplemented with 10% CCS containing 5 μg/mL polybrene and lentivirus at a multiplicity of infection (MOI) 50. Twenty-four hours after infection, fresh medium was added, and cells were trypsinized and replated every 3 d to avoid confluency.

DR-GFP assay

$Pim1^{DR-GFP/DR-GFP}$ mice (Kass et al. 2013) were crossed with $Rad50^{+/46}$, and heterozygous $Pim1^{+/DR-GFP}$ $Rad50^{+/46}$ and $Pim1^{+/DR-GFP}$ $Rad50^{+/+}$ primary skin fibroblast cultures were established. To deliver I-SceI and monitor only the I-SceI-expressing cells, we inserted and IRES-hCD4 cassette into the

retroviral vector pMX-ISceI (gift from Fred Alt). I-SceI-hCD4-expressing retrovirus produced in Phoenix cells were used to infect primary cultures in the presence of 5 μg/mL polybrene for 24 h. Seventy-two hours after the infection, cells were harvested, stained with anti-CD4 PE-Cy5 (BD-Pharmingen), and analyzed by flow cytometry. The number of GFP-positive cells was expressed as a ratio to the CD4-positive (infected) cells.

Hematopoietic lineage analysis

Hematopoietic lineages were determined as previously described (Brenet et al. 2013). Briefly, bone marrow single-cell suspensions prepared from both back legs were depleted of lineage-positive cells using a lineage cell depletion kit (Miltenyi Biotec) and simultaneously stained with different antibodies. Hematopoietic populations were identified as follows: long-term HSCs, LKS⁺ CD34⁻Flk2⁻; short-term HSCs, LKS⁺ CD34⁺ Flk2⁻; MPPs, LKS⁺ CD34⁺ Flk2⁺; CMPs, LKS⁻ CD34⁺ FcR^low; granulocyte macrophage progenitors, LKS⁻ CD34⁺ FcR⁺; and megakaryocyte erythroid progenitors, LKS⁻ CD34⁻ FcR⁻. The CLP population was defined as LKS⁺ Flk2⁺, IL7Rα⁺. DAPI was used to exclude dead cells during flow cytometric analysis.

MPPs were enumerated using the day 13 CFU-S assay. In brief, recipient mice were lethally irradiated and injected with bone marrow cells. Spleens were isolated 13 d after transplantation and fixed in Bouin's solution, and macroscopic colonies were counted.

Histological sample preparation, staining, and analysis

Tissue samples for histological analyses were fixed overnight at 4°C with 4% paraformaldehyde, rinsed, stored at 4°C in 70% ethanol, and then processed for paraffin embedding. Eight-micrometer sections were prepared, and slides were processed and stained at the Memorial Sloan-Kettering molecular cytogenetics core facility for hematoxylin and eosin (H&E), TUNEL, anti-VASA, anti-SYCP3, and anti-PLZF.

H&E-stained and immunohistochemically stained slides were digitally scanned using a Mirax scanner. TUNEL staining was quantified relative to the total area using standardized color filter settings in the Metamorph image analysis software. Anti-PLZF- and anti-SYCP3-positive cells per tubule were manually scored from at least 25 tubules per testis.

References

Adelman CA, De S, Petrini JH. 2009. Rad50 is dispensable for the maintenance and viability of postmitotic tissues. *Mol Cell Biol* **29:** 483–492.

Barlow C, Hirotsune S, Paylor R, Liyanage M, Eckhaus M, Collins F, Shiloh Y, Crawley JN, Ried T, Tagle D, et al. 1996. Atm-deficient mice: A paradigm of ataxia telangiectasia. *Cell* **86:** 159–171.

Baudat F, Manova K, Yuen JP, Jasin M, Keeney S. 2000. Chromosome synapsis defects and sexually dimorphic meiotic progression in mice lacking Spo11. *Mol Cell* **6:** 989–998.

Bender CF, Sikes ML, Sullivan R, Huye LE, Le Beau MM, Roth DB, Mirzoeva OK, Oltz EM, Petrini JH. 2002. Cancer predisposition and hematopoietic failure in Rad50(S/S) mice. *Genes Dev* **16:** 2237–2251.

Brenet F, Kermani P, Spektor R, Rafii S, Scandura JM. 2013. TGFβ restores hematopoietic homeostasis after myelosuppressive chemotherapy. *J Exp Med* **210:** 623–639.

Bressan DA, Baxter BK, Petrini JH. 1999. The Mre11-Rad50-Xrs2 protein complex facilitates homologous recombination-based double-strand break repair in *Saccharomyces cerevisiae*. *Mol Cell Biol* **19:** 7681–7687.

Buaas FW, Kirsh AL, Sharma M, McLean DJ, Morris JL, Griswold MD, de Rooij DG, Braun RE. 2004. Plzf is required in adult male germ cells for stem cell self-renewal. *Nat Genet* **36:** 647–652.

Cerami E, Gao J, Dogrusoz U, Gross BE, Sumer SO, Aksoy BA, Jacobsen A, Byrne CJ, Heuer ML, Larsson E et al. 2012. The cBio cancer genomics portal: An open platform for exploring multidimensional cancer genomics data. *Cancer discovery* **2:** 401–404.

Costoya JA, Hobbs RM, Barna M, Cattoretti G, Manova K, Sukhwani M, Orwig KE, Wolgemuth DJ, Pandolfi PP. 2004. Essential role of Plzf in maintenance of spermatogonial stem cells. *Nat Genet* **36:** 653–659.

de Jager M, van Noort J, van Gent DC, Dekker C, Kanaar R, Wyman C. 2001. Human Rad50/Mre11 is a flexible complex that can tether DNA ends. *Mol Cell* **8:** 1129–1135.

de Jager M, Trujillo KM, Sung P, Hopfner KP, Carney JP, Tainer JA, Connelly JC, Leach DR, Kanaar R, Wyman C. 2004. Differential arrangements of conserved building blocks among homologs of the Rad50/Mre11 DNA repair protein complex. *J Mol Biol* **339:** 937–949.

Demuth I, Frappart PO, Hildebrand G, Melchers A, Lobitz S, Stockl L, Varon R, Herceg Z, Sperling K, Wang ZQ, et al. 2004. An inducible null mutant murine model of Nijmegen breakage syndrome proves the essential function of NBS1 in chromosomal stability and cell viability. *Hum Mol Genet* **13:** 2385–2397.

Dull T, Zufferey R, Kelly M, Mandel RJ, Nguyen M, Trono D, Naldini L. 1998. A third-generation lentivirus vector with a conditional packaging system. *J Virol* **72:** 8463–8471.

Duursma AM, Driscoll R, Elias JE, Cimprich KA. 2013. A role for the MRN complex in ATR activation via TOPBP1 recruitment. *Mol Cell* **50:** 116–122.

Foster SS, De S, Johnson LK, Petrini JH, Stracker TH. 2012. Cell cycle- and DNA repair pathway-specific effects of apoptosis on tumor suppression. *Proc Natl Acad Sci* **109:** 9953–9958.

Frappart PO, Tong WM, Demuth I, Radovanovic I, Herceg Z, Aguzzi A, Digweed M, Wang ZQ. 2005. An essential function for NBS1 in the prevention of ataxia and cerebellar defects. *Nat Med* **11:** 538–544.

Gonzalez-Barrera S, Cortes-Ledesma F, Wellinger RE, Aguilera A. 2003. Equal sister chromatid exchange is a major mechanism of double-strand break repair in yeast. *Mol Cell* **11:** 1661–1671.

Gupta GP, Vanness K, Barlas A, Manova-Todorova KO, Wen YH, Petrini JH. 2013. The Mre11 complex suppresses oncogene-driven breast tumorigenesis and metastasis. *Mol Cell* **52:** 353–365.

Hartsuiker E, Vaessen E, Carr AM, Kohli J. 2001. Fission yeast Rad50 stimulates sister chromatid recombination and links cohesion with repair. *EMBO J* **20:** 6660–6671.

He H, Wang Y, Guo X, Ramchandani S, Ma J, Shen MF, Garcia DA, Deng Y, Multani AS, You MJ, et al. 2009. Pot1b deletion and telomerase haploinsufficiency in mice initiate an ATR-dependent DNA damage response and elicit phenotypes resembling dyskeratosis congenita. *Mol Cell Biol* **29:** 229–240.

He J, Shi LZ, Truong LN, Lu CS, Razavian N, Li Y, Negrete A, Shiloach J, Berns MW, Wu X. 2012. Rad50 zinc hook is important for the Mre11 complex to bind chromosomal DNA double-stranded breaks and initiate various DNA damage responses. *J Biol Chem* **287:** 31747–31756.

Hockemeyer D, Palm W, Wang RC, Couto SS, de Lange T. 2008. Engineered telomere degradation models dyskeratosis congenita. *Genes Dev* **22:** 1773–1785.

Hohl M, Kwon Y, Galvan SM, Xue X, Tous C, Aguilera A, Sung P, Petrini JH. 2011. The Rad50 coiled-coil domain is indispensable for Mre11 complex functions. *Nat Struct Mol Biol* **18:** 1124–1131.

Hopfner KP, Craig L, Moncalian G, Zinkel RA, Usui T, Owen BA, Karcher A, Henderson B, Bodmer JL, McMurray CT, et al. 2002. The Rad50 zinc-hook is a structure joining Mre11 complexes in DNA recombination and repair. *Nature* **418:** 562–566.

Kass EM, Helgadottir HR, Chen CC, Barbera M, Wang R, Westermark UK, Ludwig T, Moynahan ME, Jasin M. 2013. Double-strand break repair by homologous recombination in primary mouse somatic cells requires BRCA1 but not the ATM kinase. *Proc Natl Acad Sci* **110:** 5564–5569.

Lammens K, Bemeleit DJ, Mockel C, Clausing E, Schele A, Hartung S, Schiller CB, Lucas M, Angermuller C, Soding J, et al. 2011. The Mre11:Rad50 structure shows an ATP-dependent molecular clamp in DNA double-strand break repair. *Cell* **145:** 54–66.

Lim HS, Kim JS, Park YB, Gwon GH, Cho Y. 2011. Crystal structure of the Mre11–Rad50–ATPγS complex: Understanding the interplay between Mre11 and Rad50. *Genes Dev* **25:** 1091–1104.

Liu P, Jenkins NA, Copeland NG. 2003. A highly efficient recombineering-based method for generating conditional knockout mutations. *Genome Res* **13:** 476–484.

Lois C, Hong EJ, Pease S, Brown EJ, Baltimore D. 2002. Germline transmission and tissue-specific expression of transgenes delivered by lentiviral vectors. *Science* **295:** 868–872.

Luo G, Yao MS, Bender CF, Mills M, Bladl AR, Bradley A, Petrini JH. 1999. Disruption of mRad50 causes embryonic stem cell lethality, abnormal embryonic development, and sensitivity to ionizing radiation. *Proc Natl Acad Sci* **96:** 7376–7381.

Marquardt JU, Thorgeirsson SS. 2010. Stem cells in hepatocarcinogenesis: Evidence from genomic data. *Semin Liver Dis* **30:** 26–34.

Martinez P, Thanasoula M, Carlos AR, Gomez-Lopez G, Tejera AM, Schoeftner S, Dominguez O, Pisano DG, Tarsounas M, Blasco MA. 2010. Mammalian Rap1 controls telomere function and gene expression through binding to telomeric and extratelomeric sites. *Nat Cell Biol* **12:** 768–780.

Maryanovich M, Oberkovitz G, Niv H, Vorobiyov L, Zaltsman Y, Brenner O, Lapidot T, Jung S, Gross A. 2012. The ATM-

BID pathway regulates quiescence and survival of haematopoietic stem cells. *Nat Cell Biol* **14:** 535–541.

Milman N, Higuchi E, Smith GR. 2009. Meiotic DNA double-strand break repair requires two nucleases, MRN and Ctp1, to produce a single size class of Rec12 (Spo11)-oligonucleotide complexes. *Mol Cell Biol* **29:** 5998–6005.

Morales M, Theunissen JW, Kim CF, Kitagawa R, Kastan MB, Petrini JH. 2005. The Rad50S allele promotes ATM-dependent DNA damage responses and suppresses ATM deficiency: Implications for the Mre11 complex as a DNA damage sensor. *Genes Dev* **19:** 3043–3054.

Morales M, Liu Y, Laiakis EC, Morgan WF, Nimer SD, Petrini JH. 2008. DNA damage signaling in hematopoietic cells: A role for Mre11 complex repair of topoisomerase lesions. *Cancer Res* **68:** 2186–2193.

Moreno-Herrero F, de Jager M, Dekker NH, Kanaar R, Wyman C, Dekker C. 2005. Mesoscale conformational changes in the DNA-repair complex Rad50/Mre11/Nbs1 upon binding DNA. *Nature* **437:** 440–443.

Neale MJ, Pan J, Keeney S. 2005. Endonucleolytic processing of covalent protein-linked DNA double-strand breaks. *Nature* **436:** 1053–1057.

Rambo RP, Tainer JA. 2010. Improving small-angle X-ray scattering data for structural analyses of the RNA world. *RNA* **16:** 638–646.

Reina-San-Martin B, Nussenzweig MC, Nussenzweig A, Difilippantonio S. 2005. Genomic instability, endoreduplication, and diminished Ig class-switch recombination in B cells lacking Nbs1. *Proc Natl Acad Sci* **102:** 1590–1595.

Sakai K, Miyazaki J. 1997. A transgenic mouse line that retains Cre recombinase activity in mature oocytes irrespective of the cre transgene transmission. *Biochem Biophys Res Commun* **237:** 318–324.

Shiloh Y, Ziv Y. 2013. The ATM protein kinase: Regulating the cellular response to genotoxic stress, and more. *Nat Rev Mol Cell Biol* **14:** 197–210.

Shiotani B, Nguyen HD, Hakansson P, Marechal A, Tse A, Tahara H, Zou L. 2013. Two distinct modes of ATR activation orchestrated by Rad17 and Nbs1. *Cell reports* **3:** 1651–1662.

Spangrude GJ, Heimfeld S, Weissman IL. 1988. Purification and characterization of mouse hematopoietic stem cells. *Science* **241:** 58–62.

Stiff T, Reis C, Alderton GK, Woodbine L, O'Driscoll M, Jeggo PA. 2005. Nbs1 is required for ATR-dependent phosphorylation events. *EMBO J* **24:** 199–208.

Stout GJ, Blasco MA. 2009. Genetic dissection of the mechanisms underlying telomere-associated diseases: Impact of the TRF2 telomeric protein on mouse epidermal stem cells. *Dis Model Mech* **2:** 139–156.

Stracker TH, Petrini JH. 2011. The MRE11 complex: Starting from the ends. *Nat Rev Mol Cell Biol* **12:** 90–103.

Takubo K, Ohmura M, Azuma M, Nagamatsu G, Yamada W, Arai F, Hirao A, Suda T. 2008. Stem cell defects in ATM-deficient undifferentiated spermatogonia through DNA damage-induced cell-cycle arrest. *Cell Stem Cell* **2:** 170–182.

Teoh N, Pyakurel P, Dan YY, Swisshelm K, Hou J, Mitchell C, Fausto N, Gu Y, Farrell G. 2010. Induction of p53 renders ATM-deficient mice refractory to hepatocarcinogenesis. *Gastroenterology* **138:** 1155–1165.e2.

Theunissen JW, Petrini JH. 2006. Methods for studying the cellular response to DNA damage: Influence of the Mre11 complex on chromosome metabolism. *Methods Enzymol* **409:** 251–284.

Theunissen JW, Kaplan MI, Hunt PA, Williams BR, Ferguson DO, Alt FW, Petrini JH. 2003. Checkpoint failure and chromosomal instability without lymphomagenesis in Mre11(ATLD1/ATLD1) mice. *Mol Cell* **12:** 1511–1523.

Usui T, Petrini JH, Morales M. 2006. Rad50S alleles of the Mre11 complex: Questions answered and questions raised. *Exp Cell Res* **312:** 2694–2699.

van Noort J, van Der Heijden T, de Jager M, Wyman C, Kanaar R, Dekker C. 2003. The coiled-coil of the human Rad50 DNA repair protein contains specific segments of increased flexibility. *Proc Natl Acad Sci* **100:** 7581–7586.

Ventura A, Kirsch DG, McLaughlin ME, Tuveson DA, Grimm J, Lintault L, Newman J, Reczek EE, Weissleder R, Jacks T. 2007. Restoration of p53 function leads to tumour regression in vivo. *Nature* **445:** 661–665.

Williams RS, Moncalian G, Williams JS, Yamada Y, Limbo O, Shin DS, Groocock LM, Cahill D, Hitomi C, Guenther G, et al. 2008. Mre11 dimers coordinate DNA end bridging and nuclease processing in double-strand-break repair. *Cell* **135:** 97–109.

Williams RS, Dodson GE, Limbo O, Yamada Y, Williams JS, Guenther G, Classen S, Glover JN, Iwasaki H, Russell P, et al. 2009. Nbs1 flexibly tethers Ctp1 and Mre11-Rad50 to coordinate DNA double-strand break processing and repair. *Cell* **139:** 87–99.

Wiltzius JJ, Hohl M, Fleming JC, Petrini JH. 2005. The Rad50 hook domain is a critical determinant of Mre11 complex functions. *Nat Struct Mol Biol* **12:** 403–407.

Yang YG, Saidi A, Frappart PO, Min W, Barrucand C, Dumon-Jones V, Michelon J, Herceg Z, Wang ZQ. 2006. Conditional deletion of Nbs1 in murine cells reveals its role in branching repair pathways of DNA double-strand breaks. *EMBO J* **25:** 5527–5538.

Zhang S, Yajima H, Huynh H, Zheng J, Callen E, Chen HT, Wong N, Bunting S, Lin YF, Li M, et al. 2011. Congenital bone marrow failure in DNA-PKcs mutant mice associated with deficiencies in DNA repair. *J Cell Biol* **193:** 295–305.